Nanoscale mechanics of antiferromagnetic domain walls

Natascha Hedrich [1], Kai Wagner [1], Oleksandr V. Pylypovskyi [2], Brendan J. Shields [1], Tobias Kosub[2], Denis D. Sheka [3], Denys Makarov [2]✉ and Patrick Maletinsky [1]✉

Antiferromagnets can encode information in their ordered magnetic structure, providing the basis for future spintronic devices[1-3]. The control and understanding of antiferromagnetic domain walls, which are the interfaces between domains with differing order parameter orientations, are key ingredients for advancing antiferromagnetic spintronic technologies. However, studies of the intrinsic mechanics of individual antiferromagnetic domain walls are difficult because they require sufficiently pure materials and suitable experimental approaches to address domain walls on the nanoscale. Here we nucleate isolated 180° domain walls in a single crystal of Cr_2O_3, a prototypical collinear magnetoelectric antiferromagnet, and study their interaction with topographic features fabricated on the sample. We demonstrate domain wall manipulation through the resulting engineered energy landscape and show that the observed interaction is governed by the surface energy of the domain wall. We propose a topographically defined memory architecture based on antiferromagnetic domain walls. Our results advance the understanding of domain wall mechanics in antiferromagnets.

In the few years since its inception[1], the field of antiferromagnetic spintronics[2,3] has seen substantial progress, culminating in several demonstrations of antiferromagnet-based memory devices[4-6]. The focus of these advances has been on controlling and reading the bulk Néel vector of antiferromagnets[7] and their domains[8], whereas the study and direct control of individual antiferromagnetic domain walls (DWs) has received much less attention. DWs are of particular relevance to the field, as they carry essential information on the magnetic microstructure of a material[9,10], can have fundamentally different properties from the interior of domains[11,12], and delimit logical bits in magnetic memory devices[13]. Furthermore, and akin to ferromagnet-based DW logic[14], the understanding and control of antiferromagnetic DWs could inform future approaches to antiferromagnetic spintronics architectures.

In this work, we achieve an important step towards harnessing antiferromagnetic DWs for spintronics applications and thereby gain valuable insights into DW physics in antiferromagnets. Specifically, we realize antiferromagnetic DWs whose morphologies are governed by DW energy minimization and sample geometry, a key result that we obtain by direct, real-space imaging of antiferromagnetic DW trajectories with nanoscale resolution.

We demonstrate these results for the case of Cr_2O_3, a uniaxial, magnetoelectric antiferromagnet that orders at room temperature ($T_{Néel} = 307$ K) (ref. [15]). The magnetoelectric properties of Cr_2O_3 allow for local control of the Néel vector **L** through the simultaneous application of electric and magnetic fields[5,15]. In addition, symmetry breaking at the surface of Cr_2O_3 leads to a roughness-insensitive, uncompensated surface magnetic moment that is linked directly to the underlying bulk Néel vector[16,17], which can thereby be read out[18]. These combined properties render Cr_2O_3 particularly interesting for antiferromagnetic spintronics[2,6].

To address DW physics in Cr_2O_3, we employ nanoscale magnetic imaging that uses a single nitrogen vacancy (NV) electron spin in diamond as a scanning probe magnetometer[19]. NV magnetometry is among the few nanoscale imaging methods for antiferromagnets[10,20-22]; it detects stray magnetic fields that result from uncompensated magnetic moments to address antiferromagnetic order. Such moments can generally result on surfaces[17] or from spatial variations of the Néel vector[20,23] and are thereby particularly suitable for studying antiferromagnetic DWs. Here, we exploit the surface magnetic moments of Cr_2O_3 (ref. [16]) for imaging.

We perform our experiments on a (0001)-oriented Cr_2O_3 single crystal that has a thickness of 1 mm and millimetre-scale lateral dimensions. To obtain position markers and a measurable magnetic stray field from the sample, even from uniformly ordered domains, we pattern a grid of micron-scale mesas (Fig. 1a, inset) with mean thickness $\bar{t} = (166 \pm 4)$ nm and width $\bar{w} = (2.4 \pm 0.3)$ μm on the sample surface (Methods). We induce magnetic domains in the Cr_2O_3 sample via magnetoelectric field cooling[15] across $T_{Néel}$. Specifically, we apply collinear magnetic and electric bias fields along the surface normal with $B_{bias} = 550$ mT and $E_{bias} = \pm 0.75$ MV m^{-1}, and we use a split-gate capacitor to invert E_{bias} between two halves of the sample. We find this method of nucleation to be repeatable, reversible and necessary to observe DWs in the otherwise mono-domain sample (Supplementary Section II).

We show a representative NV magnetometry image of the sample obtained at room temperature and in a weak bias magnetic field ($B_{NV} = 1.6$ mT) applied along the NV axis to achieve quantitative imaging[19] (Fig. 1b). The data show stray magnetic fields emerging from a nucleated DW and from two mesas located on adjacent antiferromagnetic domains. From an analytical fit to the stray field across the mesa edges, we extract mean surface magnetizations $\sigma_m = \pm 2.1 \pm 0.3)\mu_B$ nm^{-2} (where μ_B is the Bohr magneton and the two signs apply to the different mesas), which are consistent with other measurements[21,24,25] and theoretical expectations[26]. We confirm that these data are connected to the bulk antiferromagnetic order through temperature-dependent measurements, $\sigma_m(T)$, where we observe that σ_m vanishes near $T_{Néel}$ (ref. [15]) (Supplementary Sections IV and VII).

The DW we observe constitutes an interface between regions of oppositely aligned Néel vector, **L**, through which **L** rotates by 180° over a characteristic length scale of $2\ell_m = 2\sqrt{\mathcal{A}/\mathcal{K}}$ (Fig. 1c),

[1]Department of Physics, University of Basel, Basel, Switzerland. [2]Helmholtz-Zentrum Dresden-Rossendorf e.V., Institute of Ion Beam Physics and Materials Research, Dresden, Germany. [3]Taras Shevchenko National University of Kyiv, Kyiv, Ukraine. ✉e-mail: d.makarov@hzdr.de; patrick.maletinsky@unibas.ch
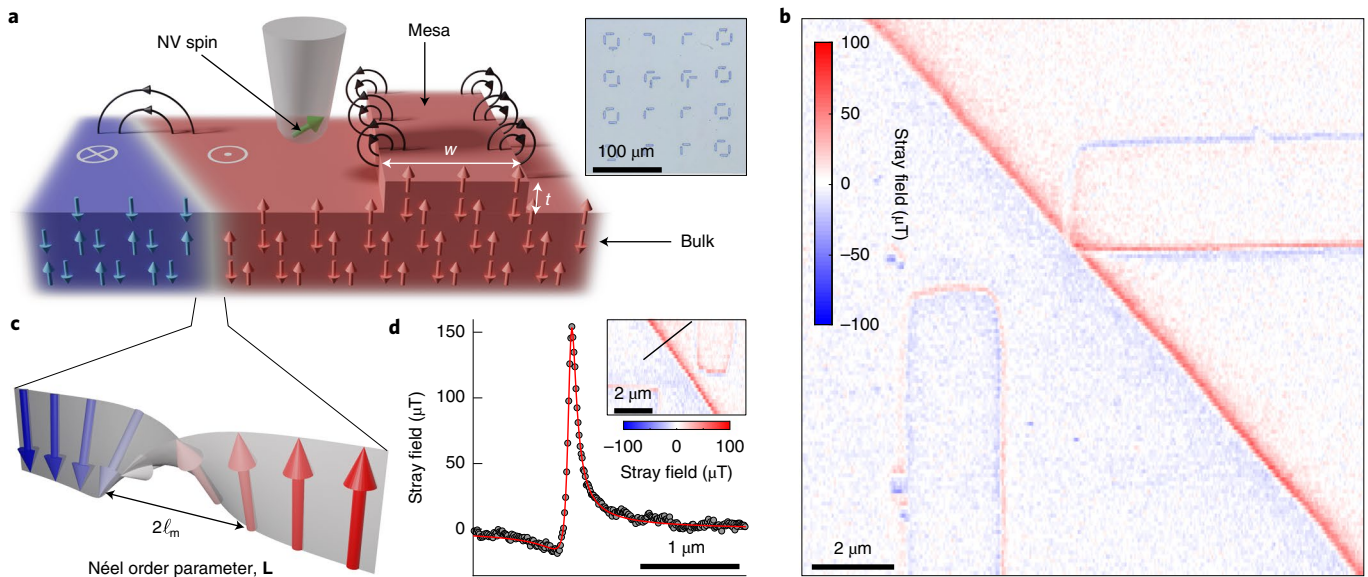
Fig. 1 | Sample structure and domain wall imaging on single-crystal antiferromagnetic Cr₂O₃. a, Schematic of the (0001)-oriented Cr_2O_3 single-crystal sample, showing the magnetic moments in two regions with oppositely oriented Néel vector **L** and the associated magnetization. Stray magnetic fields occur either on DWs or on topographic features and are measured and imaged using scanning single-spin magnetometry. The inset shows a micrograph of the mesas (of thickness $t \approx 166\,nm$) fabricated on the sample surface. **b,** Representative stray-field image obtained on the surface of the sample on a section that contains two mesas and a DW nucleated by magnetoelectric cooling. **c,** Schematic of the Néel vector evolution across the DW of width $2\ell_m$. **d,** Line cut of the magnetic field measured across the antiferromagnetic DW. From a fit to the data (red), we determine an upper bound for the magnetic length $\ell_m \lesssim 32\,nm$.

where $\mathcal{A}$ and $\mathcal{K}$ are the exchange stiffness and magnetic anisotropy[9]. We perform analytical fits to the magnetic stray field measured across the DW (Fig. 1d) to determine a room temperature upper bound of $\ell_m \lesssim 32\,nm$, which is consistent with theoretical estimates (Supplementary Section VII). Strikingly, we find the DWs away from the mesas to be smooth and straight over length scales of tens of microns (Fig. 1b and Supplementary Fig. 2), and do not observe a correlation between DW orientation and crystallographic directions of the sample.

When a DW crosses a mesa, however, we observe considerable deviations from such straight DW paths; these deviations are similar to the refraction of a light beam as described by Snell's law in geometrical optics (Fig. 2a). Indeed, the crossing of the DW through the mesa incurs an energy cost that is directly proportional to the increase in DW surface area resulting from the non-zero mesa height t. The DW then assumes a path that minimizes its surface area (and thereby its surface energy) and takes into account the local change in topography. To further support this picture, we map 17 instances of such refraction-like behaviour for a wide range of DW incidence angles, $\theta_1 \in \{\sim 20°...\sim 70°\}$ (Fig. 2b). We determine θ_1 by the DW direction off the mesa and define the angle θ_2 to be the DW direction at the centre of the mesa (Fig. 2b, inset). Similar to Snell's law, we find a linear behaviour of $\sin \theta_1 / \sin \theta_2 = 1.16 \pm 0.04$.

To obtain further insight into the observed DW mechanics, we perform spin lattice simulations[27] that take into account nearest-neighbour antiferromagnetic exchange interactions, single-site anisotropy and the sample geometry (Methods). We then obtain the equilibrium DW configuration through energy minimization of the spin lattice. The simulated DW profile on the sample surface (Fig. 2a, inset) is in excellent agreement with the experimental data, and simulations for varying incidence angles confirm the experimentally observed linear relationship between $\sin \theta_1$ and $\sin \theta_2$ (Fig. 2b).

Our numerical results inspired an analytic ansatz for the DW profile in which we use a variational procedure to relate key parameters of the DW morphology to the mesa geometry (Supplementary

Section VIII). This analysis yields an analytic expression for $n_{mesa} := \sin \theta_1 / \sin \theta_2$ (Fig. 2b, dashed line), where for small angles $\theta_1 \ll 1$ we find $n_{mesa} = 1 + 3.1(t/w)$ and additional terms $\mathcal{O}(\theta_1^2)$. Although Snell's law offers a useful analogue to the observed phenomena, this result also highlights distinctions between the two. In particular, whereas the former arises from the principle of least action alone, the DW trajectory is also determined by the DW position in the bulk of the sample, which manifests in the existence of higher-order contributions of θ_1 to n_{mesa}.

Strikingly, the simulated DW trajectories also reproduce the marked bending of the DW towards the mesa edge normal, which results in an S-shaped distortion from the otherwise straight DW profile (Fig. 2a). This distortion arises from the minimization of the exchange interaction by normal incidence of DWs to surfaces (in this case, the mesa sides)[9]. This, together with the overall DW energy minimization, fully explains the observed DW trajectory on the mesa. Our simulation also yields the three-dimensional morphology of the DW crossing the mesa (Fig. 2c), and shows how the mesa-induced distortion of the DW transitions towards the planar bulk DW shape over a characteristic length scale of t_B. Through our analytic analysis, we find $t_B \approx 0.34w$, which yields $t_B = 0.82\,\mu m$ for typical mesa widths.

The energy penalty for traversing a mesa also leads to DW-pinning phenomena at mesa edges. Specifically, we observe instances in which the bulk DW position that would intersect a mesa close to a corner is expelled instead from the mesa (Fig. 3a). This behaviour is well reproduced in simulations in which we force the bulk DW to lie close to a mesa corner (Fig. 3a, inset). In such a case, the mesa presents a large DW energy barrier, and so the path, which minimizes the overall energy, follows the mesa edge. The energetically favourable DW path ('refraction' or 'pinning') is therefore dependent on the mesa geometry and the location of the DW with respect to the mesa.

Importantly, we are able to de-pin the DW from a mesa corner and to place it on the mesa by using a focused laser spot to drag the DW (Fig. 3b). Such laser dragging, previously demonstrated
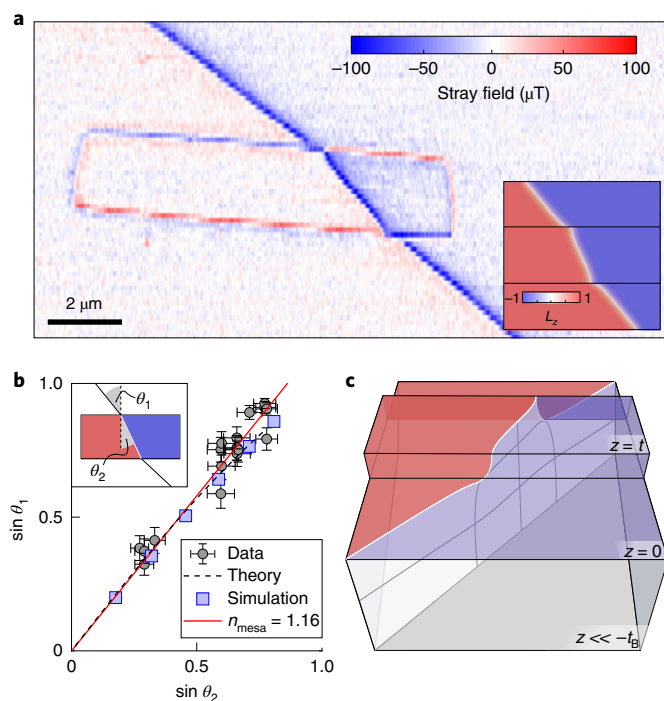
Fig. 2 | Mechanics of an antiferromagnetic domain wall. a, Stray magnetic field image of an antiferromagnetic DW crossing a mesa. The mesa deflects the DW from its otherwise straight path and leads to further DW distortion within the mesa. The inset shows that the DW trajectory as found by numerical simulation is in excellent agreement with data. **b**, Sines of the incidence and transmission angles (θ_1 and θ_2, respectively, as defined in the inset) for a DW incident on a mesa edge, as determined from 17 DW images (grey circles). The error bars are propagated based on the systematic error in position readout (Methods). The apparent linear relationship (red line) is reminiscent of Snell's law in geometrical optics and suggests DW energy minimization as the origin of the observed deflection. Numerical simulations (blue squares) and analytic calculations (dashed line) confirm the experimental findings for mesa aspect ratios $\sim \bar{t}/\bar{w}$. **c**, Full three-dimensional representation of the simulated DW surface crossing a mesa. Below the mesa, the DW twists towards the planar DW surface in the bulk over a characteristic length scale of t_B.

in the case of thin-film ferromagnets[28], is based on laser-induced heating, which locally reduces the DW energy and therefore forms a movable potential well for the DW. We find that such local DW manipulation is facilitated by increasing the sample temperature, and we therefore heat the sample to 304.5 K. We then scan the laser at elevated powers, perpendicular to the DW and in the absence of the scanning probe. We are able to reproducibly move the DW from a location on the mesa to a nearby location off the mesa and back (Fig. 3b), and thereby demonstrate the ability to achieve reliable and reversible DW manipulation.

We investigate this pinning and switching behaviour more closely through simulations. We consider the energy of a DW whose end points we pin at fixed positions x_{DW} relative to a square mesa (Fig. 3c). By varying x_{DW}, we observe three distinct equilibrium DW configurations: a straight undisturbed DW, or the DW pinned to either side of the mesa. The energy and snapshots of these configurations are shown as a function of x_{DW} (Fig. 3c). In the case of a straight DW, the DW energy increases abruptly upon crossing the mesa, and the energy step can be tuned by the mesa height. For the pinned DWs, the DW area, and hence the DW energy, increases gradually with increasing DW deflection. This observed pinning behaviour shows that the DW mimics an elastic, deformable

surface. The mechanical surface tension of the DW (energy per unit area) is determined by the material properties and sets the energy excess that results from the interaction between the DW and mesa (Supplementary Section IX). For sufficiently strong deflections, the energy of the pinned state exceeds that of a straight DW, which leads to a metastable configuration. When this happens, the application of a stimulus (for example magnetoelectric pressure or local heating) can cause a sudden relaxation of the DW state (Fig. 3c, vertical arrows). This switching process is hysteretic and controllable by the mesa height and the strength of the stimulus.

These combined results suggest a potential architecture for a scalable, DW-based antiferromagnetic memory (Fig. 3d). Specifically, we propose to employ nanoscale mesas as engineered DW pinning centres, in which binary information is encoded by the direction of **L** on a given mesa. By fabricating sufficiently thick mesas, one can energetically exclude an unpinned DW, thereby creating a bistable system in which the DW is forced to pin to one edge of the mesa or the other. The size of the antiferromagnetic memory bits is then limited solely by ℓ_m, which opens the route to bits of nanoscale dimension—a considerable improvement on currently demonstrated architectures for antiferromagnetic memories[5,6]. We demonstrate the possibility of switching and reading such bits by laser dragging and magnetometry, but integrated, all-electrical approaches could be readily envisaged. In particular, electrical gates on the mesas could be used to apply magnetoelectric pressure[16,29] for switching and to exploit the anomalous Hall effect[18] for all-electrical readout.

In conclusion, we demonstrate the deterministic generation and control of pristine DWs in a single-crystal antiferromagnet, and observe DW physics determined solely by sample geometry and the DW surface energy while defect-related DW pinning mechanisms[30] appear to be negligible. These combined achievements, together with the versatile toolset of quantum sensing[31], offer attractive avenues to exploring largely uncharted areas of DW physics, such as DW creep[32] or DW magnons in antiferromagnets[33]. Based on the generality and robustness of our modelling (Methods), we conclude that our results should extend to other achiral, uniaxial antiferromagnets. Furthermore, based on simulations, we expect the DW behaviour observed here in bulk to manifest in high-quality, thin-film samples, which is a key materials frontier that remains to be addressed in the future. Thus, our work opens multiple avenues for future research of fundamental and applied nature, be it in the form of the proposed antiferromagnetic memory devices or ultimately for the realization of DW logic[14].

Online content

Any methods, additional references, Nature Research reporting summaries, source data, extended data, supplementary information, acknowledgements, peer review information; details of author contributions and competing interests; and statements of data and code availability are available at https://doi.org/10.1038/s41567-020-01157-0.

References

1. MacDonald, A. H. & Tsoi, M. Antiferromagnetic metal spintronics. *Phil. Trans. R. Soc. A* **369**, 3098–3114 (2011).
2. Jungwirth, T., Marti, X., Wadley, P. & Wunderlich, J. Antiferromagnetic spintronics. *Nat. Nanotechnol.* **11**, 231–241 (2016).
3. Baltz, V. et al. Antiferromagnetic spintronics. *Rev. Mod. Phys.* **90**, 015005 (2018).
4. Marti, X. et al. Room-temperature antiferromagnetic memory resistor. *Nat. Mater.* **13**, 367–374 (2014).
5. Wadley, P. et al. Electrical switching of an antiferromagnet. *Science* **351**, 587–590 (2016).
6. Kosub, T. et al. Purely antiferromagnetic magnetoelectric random access memory. *Nat. Commun.* **8**, 13985 (2017).
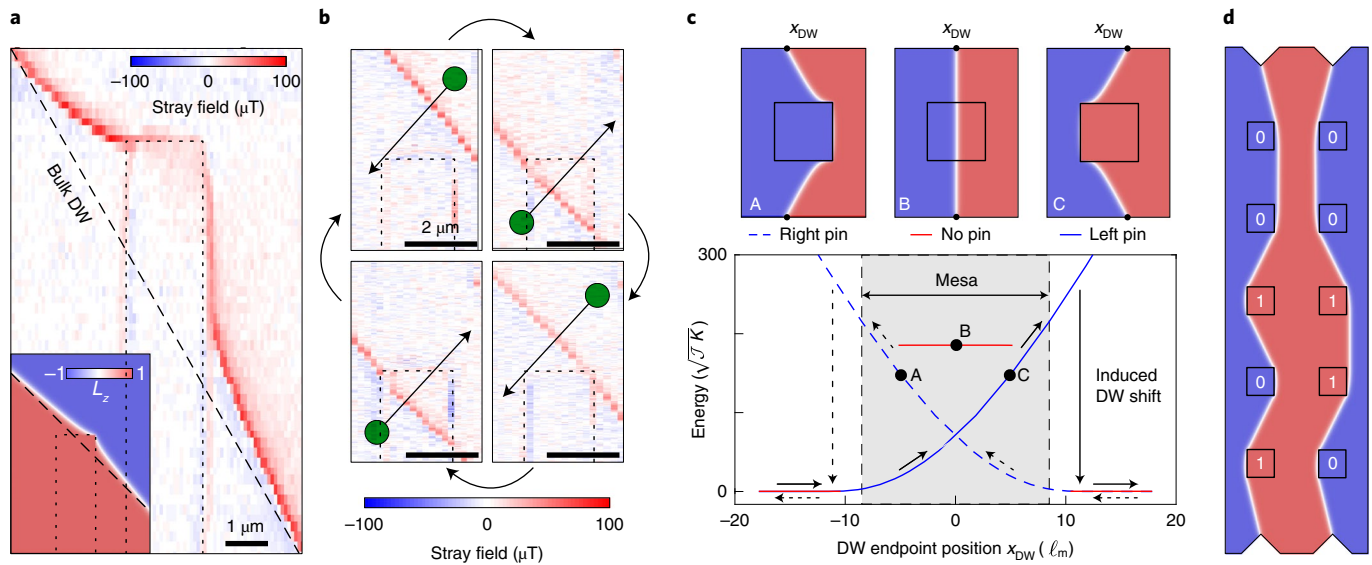
Fig. 3 | Engineered pinning and controlled manipulation of antiferromagnetic domain walls. a, Magnetic stray field image of a domain wall (DW) pinned to a mesa corner where the mesa position is highlighted by the black dashed line. The inset shows a corresponding simulation. **b**, Laser dragging of a DW across a mesa corner different from that in **a**. Green dots and straight arrows indicate the path along which the DW is dragged; curved arrows connect sequential images. **c**, The top shows simulation snapshots of the three possible (meta-)stable DW states in the vicinity of a mesa: pinned to either side of the mesa or running straight across the mesa. The bottom shows the energy of the three states (colour code and configurations shown in the top panels) as a function of the fixed DW position away from the mesa, parameterized by x_{DW}. An externally applied stimulus can cause the DW to relax to an energetically favourable state (vertical arrow). **d**, Proposal for a DW-based antiferromagnetic memory. Bit locations are defined by the mesa structures (black squares), and information is encoded by the direction of **L** on the mesa surface.

7. Song, C. et al. How to manipulate magnetic states of antiferromagnets. *Nanotechnology* **29**, 112001 (2018).
8. Fiebig, M., Fröhlich, D., Sluyterman, G. v. L. & Pisarev, R. V. Domain topography of antiferromagnetic Cr_2O_3 by second-harmonic generation. *Appl. Phys. Lett.* **66**, 2906–2908 (1995).
9. Hubert, A. & Schäfer, R. *Magnetic Domains: The Analysis of Magnetic Microstructures* Ch. 3 (Springer, 1998).
10. Weber, N. B., Ohldag, H., Gomonaj, H. & Hillebrecht, F. U. Magnetostrictive domain walls in antiferromagnetic NiO. *Phys. Rev. Lett.* **91**, 237205 (2003).
11. Kummamuru, R. K. & Soh, Y.-A. Electrical effects of spin density wave quantization and magnetic domain walls in chromium. *Nature* **452**, 859–863 (2008).
12. Jaramillo, R. et al. Microscopic and macroscopic signatures of antiferromagnetic domain walls. *Phys. Rev. Lett.* **98**, 117206 (2007).
13. Parkin, S. S. P., Hayashi, M. & Thomas, L. Magnetic domain-wall racetrack memory. *Science* **320**, 190–194 (2008).
14. Allwood, D. A. et al. Magnetic domain-wall logic. *Science* **309**, 1688–1692 (2005).
15. Brown, C. *Magnetoelectric Domains in Single Crystal Chromium Oxide*. PhD thesis, Imperial College (1969).
16. He, X. et al. Robust isothermal electric control of exchange bias at room temperature. *Nat. Mater.* **9**, 579–585 (2010).
17. Belashchenko, K. D. Equilibrium magnetization at the boundary of a magnetoelectric antiferromagnet. *Phys. Rev. Lett.* **105**, 147204 (2010).
18. Kosub, T., Kopte, M., Radu, F., Schmidt, O. G. & Makarov, D. All-electric access to the magnetic-field-invariant magnetization of antiferromagnets. *Phys. Rev. Lett.* **115**, 097201 (2015).
19. Rondin, L. et al. Magnetometry with nitrogen-vacancy defects in diamond. *Rep. Prog. Phys.* **77**, 56503 (2014).
20. Bode, M. et al. Atomic spin structure of antiferromagnetic domain walls. *Nat. Mater.* **5**, 477–481 (2006).
21. Appel, P. et al. Nanomagnetism of magnetoelectric granular thin-film antiferromagnets. *Nano Lett.* **19**, 1682–1687 (2019).

22. Cheong, S.-W., Fiebig, M., Wu, W., Chapon, L. & Kiryukhin, V. Seeing is believing: visualization of antiferromagnetic domains. *npj Quantum Mater.* **5**, 3 (2020).
23. Tveten, E. G., Müller, T., Linder, J. & Brataas, A. Intrinsic magnetization of antiferromagnetic textures. *Phys. Rev. B* **93**, 104408 (2016).
24. Brown, P. J., Forsyth, J. B., Lelièvre-Berna, E. & Tasset, F. Determination of the magnetization distribution in Cr_2O_3 using spherical neutron polarimetry. *J. Phys. Condens. Matter* **14**, 1957–1966 (2002).
25. Wornle, M. S. et al. Structure of antiferromagnetic domain walls in single-crystal Cr_2O_3. Preprint at https://arxiv.org/abs/2009.09015 (2020).
26. Shi, S., Wysocki, A. L. & Belashchenko, K. D. Magnetism of chromia from first-principles calculations. *Phys. Rev. B* **79**, 104404 (2009).
27. Pylypovskyi, O. V. & Sheka, D. D. SLaSi: a spin-lattice simulation tool. In *Book of Abstracts of the 11th EUROPT Workshop on Advances in Continuous Optimization* 11 (University of Florence, 2013).
28. Tetienne, J.-P. et al. Nanoscale imaging and control of domain-wall hopping with a nitrogen-vacancy center microscope. *Science* **344**, 1366–1369 (2014).
29. Ashida, T. et al. Isothermal electric switching of magnetization in Cr_2O_3/Co thin film system. *Appl. Phys. Lett.* **106**, 132407 (2015).
30. Lemerle, S. et al. Domain wall creep in an Ising ultrathin magnetic film. *Phys. Rev. Lett.* **80**, 849–852 (1998).
31. Degen, C. L., Reinhard, F. & Cappellaro, P. Quantum sensing. *Rev. Mod. Phys.* **89**, 035002 (2017).
32. Ferré, J. et al. Universal magnetic domain wall dynamics in the presence of weak disorder. *C. R. Phys.* **14**, 651–666 (2013).
33. Flebus, B., Ochoa, H., Upadhyaya, P. & Tserkovnyak, Y. Proposal for dynamic imaging of antiferromagnetic domain wall via quantum-impurity relaxometry. *Phys. Rev. B* **98**, 180409 (2018).

Methods

Sample preparation. The Cr_2O_3 used in this study is a commercially available, single crystal from MaTecK with a (0001) surface orientation. The original 5 mm × 5 mm × 1 mm crystal was broken into two halves along a diagonal (Supplementary Information). The sample was prepared by removing magnetic contamination (presumably resulting from the polishing process) with a 100 s Ar/Cl₂ plasma etch (ICP-RIE, Sentech) in 2 s steps. One side of the crystal was then spin-coated with a hydrogen silsesquioxane layer (FOx, Dow Corning) and subsequently developed by using electron-beam lithography to create 10 μm × 2 μm mesa masks. These mask patterns were transferred into the sample with a 100 s Ar/Cl₂ plasma etch. The masks were then removed by using hydrofluoric acid. This process results in the 166 nm tall structures (Fig. 1a, inset). For the measurements, the sample was mounted on a small Peltier element that was placed on top of an open-loop piezoelectric scanner (ANSxyz100, Attocube), which allowed us to heat the sample to ~340 K.

Nitrogen vacancy magnetometry. The NV centre is a point defect in diamond whose $S = 1$ electronic ground-state spin can be initialized and read out through optical excitation at 532 nm. Specifically, we use state-dependent fluorescence to identify the Zeeman splitting between the $|\pm 1\rangle$ spin levels by using optically detected magnetic resonance. All measurements in this study were performed by using scanning all-diamond parabolic pillars[34] that house a single NV centre and are integrated into a custom confocal imaging set-up equipped with a continuous wave 532 nm laser[35]. The measurements are performed with <10 μW of continuous-wave optical excitation, which is a factor of two lower than typical saturation powers for NVs in these parabolic scanning pillars[34]. The microwave for manipulating the NV is provided by a 30 μm gold loop antenna with a typical effective driving strength of 0.25 G at the NV. These low excitation powers (both microwave and laser) ensure that we do not disturb the DW, as confirmed by repeated scans of the DW. A small-bias magnetic field (<60 G) is applied along the NV axis by using a permanent magnet to allow for a sign-sensitive measurement of the stray magnetic fields.

Both two-dimensional magnetic field images and line scans are obtained by using a feedback technique to lock a microwave driving frequency to the instantaneous NV spin transition frequency, as described in ref. [36]. We employ single-pixel integration times that range from 0.3 s for full-field images to 5 s for individual line scans with a noise floor of $\sim 3.3\,\mu\mathrm{T}\,\sqrt{\mathrm{Hz}^{-1}}$.

Domain wall nucleation. DWs are nucleated in the otherwise mono-domain single-crystal Cr_2O_3 by using magnetoelectric cooling through the Néel temperature. A uniform magnetic field is achieved by placing two 5 cm × 5 cm × 2 cm permanent magnets adjacent to each other. The result is a nearly homogeneous magnetic field of $B \approx 550$ mT along the centre normal, as measured by a Hall probe (AS-NTM, FM302 Teslameter, Projekt Elektronik). In addition, we apply electric fields across the sample by using a split-gate capacitor that consists of two quartz plates with 100 nm Au evaporated onto the surface. The Cr_2O_3 sample is then centred onto the capacitor gap and sandwiched between the top and bottom gate together with thin mica sheets to prevent electroplating of Au onto the crystal surface (see Supplementary Information for a schematic of this set-up). The entire device is then heated to far above the Néel temperature and allowed to cool to room temperature while simultaneously ±750 V are applied between the electrodes, which leads to an electric field of $E \approx 0.75$ MV m^{-1} across the crystal. The resulting $|\mathbf{E} \cdot \mathbf{B}| = 0.41 \times 10^6$ VT m^{-1} forces the Cr_2O_3 sample into a two-domain state. The crystal can again be made mono-domain by repeating this procedure with a uniform capacitor rather than the split-gate capacitor. This process was repeated twice to show the reproducibility; each realization resulted in a different domain configuration (Supplementary Section II).

Domain wall dragging. The repeated movement of the DW is demonstrated via local heating with a laser, a process we describe as laser dragging. For this, we remove the NV scanning probe and focus the laser onto the sample surface with a beam diameter of ~420 nm. We scan the sample at a speed of roughly 80 nm s^{-1}, perpendicular to the DW, over distances exceeding 10 μm before reducing the laser power back to below 10 μW. With this method, the minimum laser power at which we have observed DW motion is 135 μW. We then re-insert the NV scanning probe and image the new DW position. These experiments were performed at a sample temperature of 304 K, which was achieved through heating with the Peltier element. This DW dragging is verified through direct measurements with the NV (Supplementary Section X).

Error analysis. We characterize our piezo scanner displacement to correct for the piezo non-linearity (Supplementary Section I). We compare the corrected mesa dimensions measured in our set-up to those measured with a Bruker Dimension 3100 atomic force microscope and obtain a 10% error. We therefore take this value to be the uncertainty in the lateral scales that factor into the error bars in Fig. 2b.

To determine the errors on the DW deflection angles, we take, as stated above, the uncertainty in the x and y distances (Δx and Δy, respectively) to be $\Delta x = \Delta y = 10\%$. Through simple error propagation, we then obtain $\delta k_{(1)} = \sqrt{2} k_{(1)} \Delta x$. Here, k (k_1) is the slope of the DW in the bulk (on the mesa),

which can then be converted to an error in $\sin(\theta_{1(2)})$ through further error propagation. This results in

$$\delta \sin(\theta_{1(2)}) = \frac{\sqrt{2} k_{(1)} \Delta x}{\left(1 + k_{(1)}^2\right)^{3/2}}, \tag{1}$$

which is plotted as the error bars in Fig. 2b. We then use a linear regression to obtain the final estimate of n_{mesa}. Further discussions of uncertainty are found throughout the Supplementary Information.

Fitting to mesa stray fields. The mesa structures etched into the surface of Cr_2O_3 play a critical role in our study as they act as sources of stray fields for characterizing the surface magnetization (σ_{m}) and NV sample spacing (d_{NV}) and for providing reference markers. For the former, we consider 29 line-cut sections, each taken over a mesa, and fit the stray field at the mesa edges by modifying a well-studied model[37] that describes the stray field as arising from line currents along the top and bottom edges of the mesa (Supplementary Information). We obtain estimates of the NV angles (θ_{NV} and ϕ_{NV}), d_{NV}, σ_{m} and the mesa edge positions, as well as their variances, through the Metropolis–Hastings algorithm (Supplementary Information). In particular, by combining the results of all 29 data sets, collected at various temperatures, we obtain reasonable estimates of the NV angles, $\theta_{\mathrm{NV}} = 60.7 \pm 2.9$ degrees and $\phi_{\mathrm{NV}} = 260.6 \pm 0.8$ degrees. We furthermore extract a mean $d_{\mathrm{NV}} = 51.4 \pm 19.2$ nm. By considering only the six measurements taken at room temperature, we determine the value for the surface moment density, $\sigma_{\mathrm{m}} = 2.1 \pm 0.3\,\mu_{\mathrm{B}}\,\mathrm{nm}^{-2}$, where the error corresponds to the standard deviation.

Fitting to domain wall stray fields. To describe the stray field of a DW in Cr_2O_3, we begin with the typical description of the evolution of the magnetic moments of the two sublattices in this collinear antiferromagnet[38,39]. For this, we assume a Bloch wall of the typical form

$$L_x = 0, \tag{2}$$

$$L_y = \mathrm{sech}(\mathrm{x}/\ell_{\mathrm{m}}), \tag{3}$$

$$L_z = \tanh(x/\ell_{\mathrm{m}}), \tag{4}$$

where ℓ_{m} is the magnetic length, as given previously. Thus, the DW profile (Fig. 1c) is determined by ℓ_{m}, which allows us to use this parameter to characterize the DW width. This form of the DW profile is then considered in the derivation of the stray field along the NV axis (Supplementary Section V).

We again use the Metropolis–Hastings algorithm to evaluate our model of the stray field with the stray field data. To do so, the NV-sample spacing, angles and surface magnetization extracted previously from the mesa fits are used as prior information. In particular, we consider the NV sample spacing on a case-by-case basis as each DW line scan is taken concurrently with a mesa line scan. The upper bound for ℓ_{m} stated previously is then obtained from extrema of the likelihood distributions at room temperature; the 98th percentile of the cumulative distribution function is selected as the upper limit on ℓ_{m}. This implies that, at room temperature, our data exclude an ℓ_{m} greater than 32 nm.

We note that for completeness, the stray field data have also been analysed under the assumption of a Néel wall, which results in a similar quality fit for slightly changed model parameters. However, the resulting DW width is consistently smaller for a Néel wall, which maintains the validity of our statement about the upper limit of ℓ_{m}, regardless of wall type.

Simulation details. The spin-lattice simulations are performed with the in-house-developed SLaSi package[27,40], which was rewritten in the CUDA (compute unified device architecture) framework. The simulations are based on a generic antiferromagnet that consists of a simple cubic lattice, which is described by the effective Hamiltonian

$$\mathcal{H} = \frac{\mathcal{J}S^2}{2}\sum_{i,i'} i \cdot i' - \frac{KS^2}{2}\sum_i (\mu_i^z)^2$$
$$+ c_{\mathrm{d}} \frac{\mu_0 g^2 \mu_{\mathrm{B}}^2 S^2}{8\pi} \sum_{i \neq j} \left[\frac{i \cdot j}{r_{ij}^3} - 3\frac{(i \cdot \mathbf{r}_{ij})(j \cdot \mathbf{r}_{ij})}{r_{ij}^5} \right]. \tag{5}$$

Here, $\mathcal{J}$ is the exchange integral, K is the easy-axis ($\mathbf{e}_z$) anisotropy, $\boldsymbol{\mu}_i$ is the unit vector representing the direction of the magnetic moment at the ith lattice site, and i' runs over the nearest neighbours of i, yielding the oppositely oriented magnetic sublattices. To represent a general antiferromagnet while approximating the properties of Cr_2O_3, we set $S = 1$, $a = 0.277$ nm, $\mathcal{J} = 2.34 \times 10^{-9}$ pJ (ref. [26]) and $K = 2.6 \times 10^{-10}$ pJ, which leads to $\ell_{\mathrm{m}} = a\sqrt{\mathcal{J}/K} = 0.83$ nm. These values allow for a reasonable scale of the sample for spin-lattice simulations and properly reproduce the effects observed in experiments. The last term in the Hamiltonian represents the dipolar interaction, which we control by the parameter $c_{\mathrm{d}} \in \{0, 1\}$. We find that dipolar interactions do not change the results of our simulations quantitatively, and therefore favour $c_{\mathrm{d}} = 0$ in the following, which is consistent with other studies.

With this, we solve the set of Landau–Lifshitz–Gilbert equations

$$\frac{d_i}{dt} = \frac{1}{\hbar S_i} \times \frac{\partial \mathcal{H}}{\partial_i} + \alpha_{Gi} \times \frac{d_i}{dt}, \tag{6}$$

where ħ is the reduced Planck's constant and $\alpha_G = 0.5$ is the Gilbert damping, by using the Runge–Kutta–Fehlberg scheme of order 4–5 with a fixed time step to find the equilibrium magnetic state when max $|d_i/dt| \rightarrow 0$. We simulate parallelepiped-shaped samples with the mesa faces coinciding with lattice planes. This is done without loss of generality, as simulations with arbitrarily oriented mesas show no significant variations.

To simulate a given bulk DW position, in particular for the study shown in Fig. 3c, we fix the equilibrium DW by notches at the sample boundaries. The initial state is defined as either a straight DW, which can cross the mesa, or a DW that is pinned at and bent around the mesa edges. The magnetization is then relaxed and its energy is compared to that of an unperturbed DW far from the mesa. The excess energy of the initial state can cause the DW to switch from a high-energy (strongly extended) state to a low-energy state, thereby imitating an induced switch due to an external stimulus. We note that the present model contains no bias to select a particular DW type (Bloch, Néel or other). The resulting equilibrium DW type in the simulations is therefore determined by the initial magnetic state that we choose before numerical relaxation and may also vary along the DW. We varied details of the initial conditions and observed no influence of the DW type on the relaxed DW trajectory.

Finally, to further investigate the robustness of our model, we performed simulations in which we lower the structural symmetry of the lattice by shifting the two magnetic sublattices that we consider by half a lattice constant with respect to each other along the main axis of the cubic lattice. We still observe results quantitatively similar to those of the original simple cubic lattice, which indicates that our model is indeed robust against variations in lattice parameters.

In conclusion, our minimal model appears to be justified as it already captures all features of the DW mechanics observed in our experiments. Furthermore, the generality of this model suggests that it should be applicable to any achiral, uniaxial antiferromagnet.

Data availability

Source data are provided with this paper. All data shown are available from Zenodo at https://doi.org/10.5281/zenodo.3941994[41].

Code availability

The spin lattice simulation software[40] used in this paper is available at http://slasi.knu.ua.

References

34. Hedrich, N., Rohner, D., Batzer, M., Maletinsky, P. & Shields, B. J. Parabolic diamond scanning probes for single-spin magnetic field imaging. *Phys. Rev. Appl.* **14**, 064007 (2020).
35. Grinolds, M. S. et al. Nanoscale magnetic imaging of a single electron spin under ambient conditions. *Nat. Phys.* **9**, 215–219 (2013).
36. Schoenfeld, R. S. & Harneit, W. Real time magnetic field sensing and imaging using a single spin in diamond. *Phys. Rev. Lett.* **106**, 030802 (2011).
37. Tetienne, J.-P. et al. The nature of domain walls in ultrathin ferromagnets revealed by scanning nanomagnetometry. *Nat. Commun.* **6**, 6733 (2015).
38. Belashchenko, K. D., Tchernyshyov, O., Kovalev, A. A. & Tretiakov, O. A. Magnetoelectric domain wall dynamics and its implications for magnetoelectric memory. *Appl. Phys. Lett.* **108**, 132403 (2016).
39. Mitsumata, C. & Sakuma, A. Generalized model of antiferromagnetic domain wall. *IEEE Trans. Magn.* **47**, 3501–3504 (2011).
40. SLaSi spin-lattice simulations package version 1.0 (RITM group, 2020); http://slasi.knu.ua
41. Hedrich, N. et al. Replication data for: Nanoscale mechanics of antiferromagnetic domain walls. *Zenodo* https://doi.org/10.5281/zenodo.3941994 (2020).

Author contributions

P.M., D.M., T.K., N.H. and B.J.S. conceived the experiment. N.H., B.J.S. and K.W. performed the NV magnetometry experiments and analysed the resulting data. N.H., K.W. and B.J.S. performed the nanofabrication. O.V.P. and D.D.S. performed the numerical simulations and analytical calculations. All authors contributed to the writing of the paper.

Competing interests

The authors declare no competing interests.

Additional information

Supplementary information The online version contains supplementary material available at https://doi.org/10.1038/s41567-020-01157-0.

Correspondence and requests for materials should be addressed to D.M. or P.M.

Peer review information *Nature Physics* thanks Christian Binek, Chunhui Du and the other, anonymous, reviewer(s) for their contribution to the peer review of this work.

Reprints and permissions information is available at www.nature.com/reprints.